IJMMM
International Journal of
Minerals, Metallurgy and Materials
矿物冶金与材料学报（英文版）

Effect of Co substitution on the structural, dielectric and optical properties of $KBiFe_2O_5$

K. Chandrakanta, R. Jena, P. Pal, Md.F. Abdullah, S.D. Kaushik, and A.K. Singh

Cite this article as:
K. Chandrakanta, R. Jena, P. Pal, Md.F. Abdullah, S.D. Kaushik, and A.K. Singh, Effect of Co substitution on the structural, dielectric and optical properties of $KBiFe_2O_5$, *Int. J. Miner. Metall. Mater.*, 28(2021), No. 11, pp. 1861-1867. https://doi.org/10.1007/s12613-020-2110-4

View the article online at SpringerLink or IJMMM Webpage.

Articles you may be interested in

Seyed Rahim Kiahosseini and Hossein Ahmadian, Effect of residual structural strain caused by the addition of Co_3O_4 nanoparticles on the structural, hardness and magnetic properties of an Al/Co_3O_4 nanocomposite produced by powder metallurgy, *Int. J. Miner. Metall. Mater.*, 27(2020), No. 3, pp. 384-390. https://doi.org/10.1007/s12613-019-1917-3

J. Celina Selvakumari, M. Ahila, M. Malligavathy, and D. Pathinettam Padiyan, Structural, morphological, and optical properties of tin(IV) oxide nanoparticles synthesized using *Camellia sinensis* extract:a green approach, *Int. J. Miner. Metall. Mater.*, 24(2017), No. 9, pp. 1043-1051. https://doi.org/10.1007/s12613-017-1494-2

Wan-liang Mi, Zhao-sen Liu, Toru Kimura, Atsunori Kamegawa, and Hai-liang Wang, Crystal structure and hydrogen storage properties of $(La,Ce)Ni_{5-x}M_x$ (M=Al, Fe, or Co) alloys, *Int. J. Miner. Metall. Mater.*, 26(2019), No. 1, pp. 108-113. https://doi.org/10.1007/s12613-019-1714-z

Zhi-yu Chang, Ping Wang, Jian-liang Zhang, Ke-xin Jiao, Yue-qiang Zhang, and Zheng-jian Liu, Effect of CO_2 and H_2O on gasification dissolution and deep reaction of coke, *Int. J. Miner. Metall. Mater.*, 25(2018), No. 12, pp. 1402-1411. https://doi.org/10.1007/s12613-018-1694-4

Yan-ping Xia, Pei-hong Wang, Shi-wei Shi, Gang He, Miao Zhang, Jian-guo Lü, and Zhao-qi Sun, Effect of oxygen partial pressure and transparent substrates on the structural and optical properties of ZnO thin films and their performance in energy harvesters, *Int. J. Miner. Metall. Mater.*, 24(2017), No. 6, pp. 675-680. https://doi.org/10.1007/s12613-017-1450-1

Hui-bin Wu, Tao Wu, Gang Niu, Tao Li, Rui-yan Sun, and Yang Gu, Effect of the frequency of high-angle grain boundaries on the corrosion performance of 5wt%Cr steel in a CO_2 aqueous environment, *Int. J. Miner. Metall. Mater.*, 25(2018), No. 3, pp. 315-324. https://doi.org/10.1007/s12613-018-1575-x

IJMMM WeChat　　QQ author group

International Journal of Minerals, Metallurgy and Materials
Volume 28, Number 11, November 2021, Page 1861
https://doi.org/10.1007/s12613-020-2110-4

Effect of Co substitution on the structural, dielectric and optical properties of $KBiFe_2O_5$

K. Chandrakanta[1)], *R. Jena*[1)], *P. Pal*[1)], *Md.F. Abdullah*[1)], *S.D. Kaushik*[2)], *and A.K. Singh*[1)]

1) Department of Physics and Astronomy, National Institute of Technology, Rourkela-769008, Odisha, India
2) UGC-DAE Consortium for Scientific Research Mumbai Centre, R-5 Shed, BARC, Mumbai-400085, India

(Received: 12 January 2020; revised: 23 May 2020; accepted: 28 May 2020)

Abstract: Cobalt (Co)-modified brownmillerite $KBiFe_2O_5$ (KBFO; [$KBiFe_{2(1-x)}Co_{2x}O_5$ (x = 0, 0.05)]) polycrystalline is synthesized following the solid-state reaction route. Rietveld refinement of X-ray diffraction data confirmed the phase purity of KBFO and $KBiFe_{1.9}Co_{0.1}O_5$ (KBFCO). The optical bandgap energy (E_g) of KBFO decreased from 1.59 to 1.51 eV because of Co substitution. The decrease in bandgap can be attributed to the tilting of the Fe–O tetrahedral structure of KBFCO. The observed room-temperature Raman peaks of KBFCO shifted by 3 cm^{-1} toward a lower wavenumber than that of KBFO. The shift in Raman active modes can be attributed to the change in the bond angles and bond lengths of the Fe–O tetrahedral structure and modification in response to oxygen deficiency in KBFO because of Co doping. Compared with that of KBFO, the frequency-dependent dielectric constant and dielectric loss of KBFCO decrease at room temperature, which is a consequence of the reduction in oxygen migration and modification in response to vibrational modes present in the sample.

Keywords: brownmillerite; rietveld refinement; Raman spectroscopy; bandgap

1. Introduction

Multiferroic materials with photovoltaic features have received considerable attention from the scientific community because of its multifunction and solar cell applications [1]. Among them, $KBiFe_2O_5$ (KBFO) is the most promising material with magnetoelectric behavior at room temperature [2]. Being an insulator and room-temperature ferroelectric material, KBFO has considerable potential to be used in memory and photovoltaic applications. Zhang *et al.* [3] reported approximately 30% photovoltaic efficiency limit for KBFO from theoretical calculations. KBFO exhibited higher photocurrent and photovoltage than the well-known multiferroic perovskite $BiFeO_3$ [4]. KBFO belongs to the brownmillerite class ($A'AB_2O_5$; A' = K, A = Bi, B = Fe) of materials with high Curie temperature (T_C, ~510°C) and Néel temperature (T_N, ~270°C) [3]. Materials belonging to the brownmillerite class exhibit inherently oxygen-deficient characteristics during its synthesis process, which play an important role in determining its electric and magnetic properties [5].

On the basis of the spectral distribution of solar energy, materials with bandgap ranging from 1.0 to 1.8 eV are suitable for light absorption [6]. This wide absorption range further enhances the excellent photovoltaic properties. Most ferroelectric materials lack this absorption range as they have a wide bandgap (>3 eV), which makes these materials inappropriate for photovoltaic applications [7]. Multiferroic materials with suitable bandgap are chosen over ferroelectric materials for photovoltaic applications because ferroelectric and magnetic properties influence the photovoltaic effect [8]. In multiferroic and photovoltaic cells, the ferroelectric polarization domain helps separate the charge carriers generated by photons and the magnetic domain helps ensure the flow of the photon-generated current produced by the ferroelectric domain. The magnetic property of multiferroic materials helps their magnetic domain and spin structure facilitate charge carrier motions. Therefore, the magnetic and ferroelectric properties and the narrow bandgap facilitate the use of KBFO in multiferroic and photovoltaic devices. To use KBFO in any versatile device application, its magnetic, electric, dielectric, and optical properties need to be tuned.

The electrical and magnetic properties, such as bandgap, dielectric constant, and magnetization, of oxide materials can be tuned by chemical pressure [9]. Moreover, the volatile nature of potassium (K) and bismuth (Bi) in KBFO makes the compound leaky. Various ways to suppress leakage in-

---

Corresponding author: A.K. Singh E-mail: singhanil@nitrkl.ac.in

clude substitution, which is the most commonly used technique to reduce leakage in certain materials [10]. Iron (B site) or bismuth (A site) can be substituted by transition metal ions, such as cobalt (Co), to induce lattice strain and lattice mismatch between host and donor and can be substituted by cations to reduce impurities and leakage in the sample [11]. To explore new functionalities, KBFO and 5% Co-doped KBFO are prepared using the solid-state reaction technique using corresponding weight percentage. Here, we preferred partial replacement of Fe with Co ion (B-site substitution) as both of them have slightly different ionic radii ($R_{\mathrm{Fe}^{3+}}$, ~0.064 nm; $R_{\mathrm{Co}^{3+}}$, ~0.06 nm). The structural, morphological, bandgap (E_g), Raman, and dielectric properties of KBFO and 5% Co-doped KBFO are investigated in detail. Our results confirm the assumption that the bandgap of KBFO can be tuned by Co doping at the Fe site.

2. Experimental

The pure and Co-doped KBFO polycrystalline samples are prepared by solid-state reaction of high-purity oxides (≥ 99.9%), i.e., K_2CO_3, Bi_2O_3, Fe_2O_3, and Co_2O_3, obtained from Sigma-Aldrich (St. Louis, MO, USA). The precursor powders with the appropriate stoichiometric proportion are mixed and ground thoroughly in an agate motor for 2 h. The ground mixture is pelletized using a hydraulic press, and the cylindrical pellets with a diameter of 10 mm are heated at 650°C for 4 h using a PID (proportional-integral-derivative)-controlled programmable silicon carbide tubular furnace. Then, the pellets are again ground and pelletized. Finally, the pellets are sintered at 700°C for 2 h. These heat treatments are conducted at a ramp rate of approximately 3°C/min. X-ray diffraction (XRD) measurement is performed at room temperature using a Rigaku diffractometer (Rigaku, Tokyo, Japan) equipped with Cu-K$_\alpha$ radiation (λ = 0.15406 nm). Then, the purity of the sample is confirmed using a Bragg–Brentano diffractometer equipped with a secondary Ni filter. The XRD measurement is performed over a wide range of Bragg angles (i.e., 10° to 70°) with a step size of 0.02° and a scan rate of 3°·min^{-1}. Dielectric measurement is performed as a function of frequency (100 Hz to 1 MHz) at room temperature using a Wayne Kerr 6500B impedance analyzer. A scanning electron microscope (SEM; JEOL JSM-6480LV) is used to characterize the microstructure of KBFO and $KBiFe_{1.9}Co_{0.1}O_5$ (KBFCO). To analyze the optical properties of KBFO and KBFCO, UV–visible absorbance is recorded using a UV–visible spectrophotometer (UV2450). Room-temperature Raman spectra are recorded using a confocal Raman microscope (WITec Alpha300 R). A solid-state laser (532 nm) is used as an excitation source.

3. Results and discussions

3.1. XRD and structural analysis

Fig. 1(a) shows the Rietveld-refined XRD patterns of the KBFO and KBFCO polycrystalline samples observed at room temperature. The XRD patterns of both samples are refined by the Rietveld refinement method using the FullProf Suite software [12]. The refined XRD peaks of Co-doped KBFO match well with that of pure KBFO, confirming the phase purity of the samples [13]. Notably, both samples belong to the brownmillerite class of polycrystalline with a

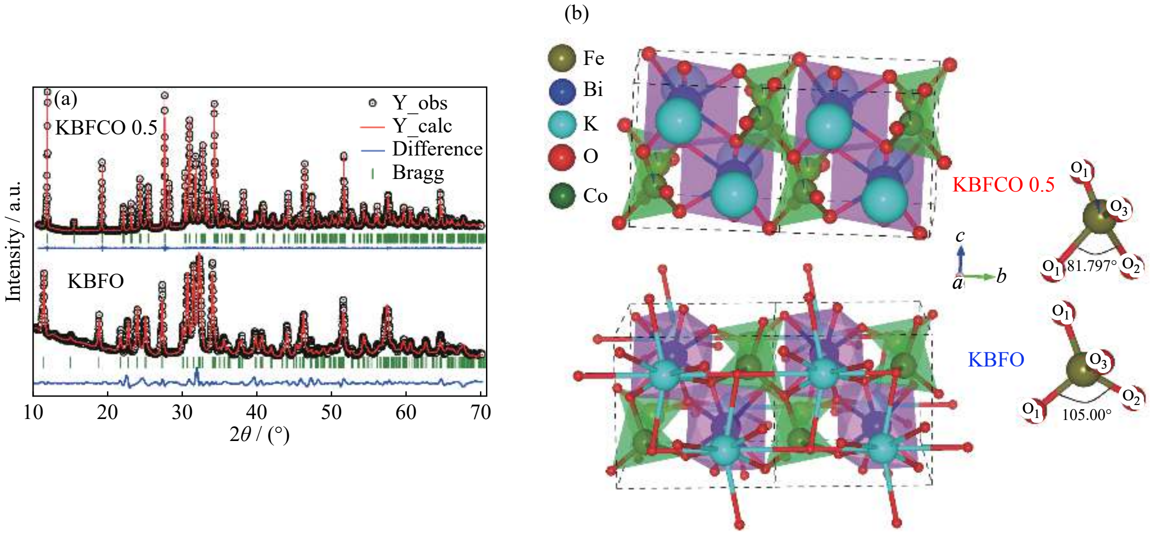

Fig. 1. (a) Room-temperature Rietveld-refined XRD patterns of KBFO (lower half) and KBFCO (upper half). The open circles denote the observed XRD patterns, the red lines denote the calculated XRD patterns obtained using the Rietveld software, the blue lines denote the differences between the observed and calculated XRD patterns, and the green lines denote the observed Bragg planes. (b) Monoclinic crystal structure of KBFCO and KBFO with their Fe–O_4 tetrahedral structure. The O_1–Fe–O_2 bond angle of each sample is highlighted.

monoclinic crystal structure and P2/c space group. The lattice parameter values of χ^2, R_{wp}, and R_p are 9.8, 30.5, and 32.3 for KBFO and 3.2, 9.01, and 14.1 for KBFCO, respectively, as obtained by Rietveld refinement of the XRD data given in Table 1. Fig. 1(b) shows the refined monoclinic crystal structure (extracted using the VESTA software) of both pure and Co-doped KBFO with their corresponding distorted FeO_4 tetrahedral structures with different bond angles. The KBFO crystal structure is simply an alternating block of $[Fe_2O_3]$ and $[(K,Bi)O_2]$ loosely connected by corner-sharing oxygen atoms between FeO_4 and BiO_6 polyhedra. Each Fe^{3+} ion is distorted and has four Fe–O tetrahedral bonds [14]. The corner-sharing FeO_4 tetrahedrons are connected by tetrahedral chains along the "*b*" direction (Fig. 2). As Co is substituted at the Fe site, the FeO_4 tetrahedral structure is compressed by 6.4%, which changes the interatomic distances of the Fe–O, Fe–Bi, and Bi–O bonds, as well as the O_1–Fe–O_2, O_1–Fe–O_1, and O_3–Fe–O_2 bond angles, listed in Table 2.

Table 1. Structural parameters obtained by Rietveld analysis

Samples	*a* / nm	*b* / nm	*c* / nm	χ^2	R_{wp}	R_p
KBFO	0.7894	0.5975	0.5725	9.8	30.5	32.3
KBFCO	0.7889	0.5971	0.5725	3.2	9.01	14.1

Table 2. Structural parameters (bond lengths and bond angles)

Sample	Bond parameters / nm				Bond angle / (°)		
	Fe–O_1	Fe–O_2	Fe–O_3	Bi–O_1	O_1–Fe–O_1	O_1–Fe–O_2	O_3–Fe–O_2
KBFO	0.1844	0.1893	0.2189	0.2705	109.603	105.00	104.50
KBFCO	0.1430	0.2498	0.1823	0.3100	117.090	81.797	129.281

3.2. SEM Analysis

Surface morphology is examined using the SEM micrographs of both pure and Co-doped KBFO samples (shown in Fig. 2). The average grain size of both pure and Co-doped KBFO samples varies within the range of 2–3 µm. Pure KBFO grains are agglomerated with random orientation forming a continuous grain boundary, whereas Co-doped KBFO grains are distinct with less agglomeration. This finding can be attributed to the mismatch between ionic radii of Co^{3+} and Fe^{3+} [15]. To obtain better insights into the chemical constituents of both pure and Co-doped samples, we used the energy-dispersive X-ray spectroscopy (EDS) technique, as shown in Figs. 2(c) and 2(d). EDS analysis provided additional results concerning the chemical elements, which we have taken into account to synthesize the as-required samples. The chemical composition was confirmed by EDS analysis, and the molar ratio of K/Bi/Fe is 1:1:2 in atomic weight percent. The extracted elements with their corresponding atomic weight percents are shown in the insets of Figs. 2(c) and 2(d).

3.3. Bandgap Analysis

The UV–visible spectra of the synthesized KBFO and Co-doped KBFO samples are shown in Fig. 3. The inset of Fig. 3 shows the absorbance versus wavelength (300–800 nm) plot of both samples. The optical bandgap energy is calculated by the relation proposed by Wood and Tauc [16] expressed as follows:

$$\alpha h\nu = A\left(h\nu - E_g\right)^n \tag{1}$$

where α is the optical absorption coefficient, $h\nu$ is the energy, A is a constant, E_g is the optical bandgap, and n is a constant that signifies different types of electronic transitions. The Tauc plot depicts the variation between $(\alpha h\nu)^2$ and $h\nu$ (Fig. 3). From the linear region of the Tauc plot, the values of the op-

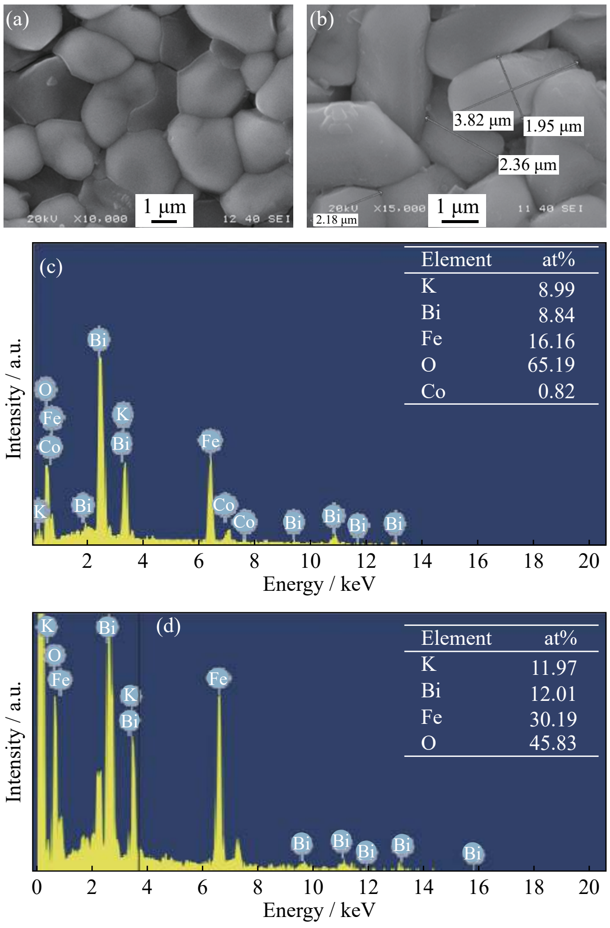

(c)

Element	at%
K	8.99
Bi	8.84
Fe	16.16
O	65.19
Co	0.82

(d)

Element	at%
K	11.97
Bi	12.01
Fe	30.19
O	45.83

Fig. 2. SEM micrographs of (a) KBFO and (b) Co-doped KBFO. EDS spectra of (c) KBFCO and (d) KBFO, with the insets showing the chemical elements and its corresponding atomic weight percents.

tical bandgap energy (E_g) of pure and Co-doped KBFO are determined to be 1.59 and 1.51 eV, respectively. The low bandgap energy of KBFO can be attributed to the FeO_4 tetrahedral structure having a low crystal-field splitting energy [13,17]. As Co is doped at the Fe site, the bandgap energy is decreased. The observed bandgap (1.51 eV) of Co-doped KBFO is the lowest reported energy bandgap in the brownmillerite class. The reduction in bandgap due to Co doping is related to the distortion generated in the FeO_4 tetrahedral structure, which further splits the crystal-field energy. Moreover, the decrease in the grain size of Co changes the Fe–O bond lengths and Fe–O–Fe bond angles, thereby reducing the bandgap [18].

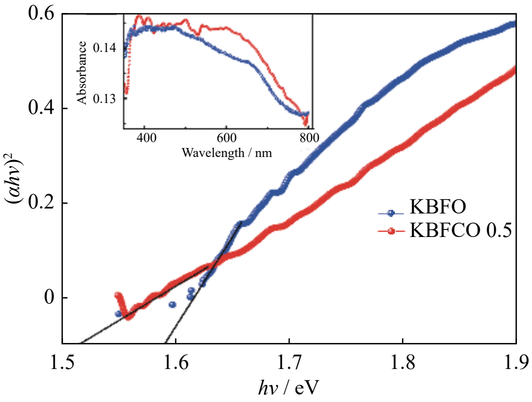

Fig. 3. Tauc plot of the KBFO and KBFCO samples. The inset shows the absorbance versus wavelength plot of both samples.

3.4. Raman studies

Fig. 4(a) shows the observed room-temperature Raman spectra of both pure and Co-doped KBFO. Raman spectroscopy is an effective tool for extracting information regarding structural changes, molecular vibrations, defect states, spin–phonon coupling, and oxygen vacancies of the materials [19]. Lorentzian fitting of the room-temperature Raman spectra is shown in Fig. 4(b). Here, we fitted the experimental Raman data with the Lorentzian function to extract the possible Raman active modes in both pure and Co-doped KBFO samples. A total of 14 Raman peaks or vibrational modes are extracted from the room-temperature Raman data using the Lorentzian fitting function. Group theory predicts a total of 27 possible Raman active modes ($12A_g$ + $15B_g$) present at room temperature in the KBFO sample [20]. Where A_g is symmetric, and B_g is anti-symmetric irreducible vibrational modes with singly degenerate, respectively. As shown in Fig. 4(a), the Raman peaks of Co-doped KBFO shifted toward a lower wavenumber (redshift) than that of pure KBFO. To observe the shift, we highlighted the lower wavenumber ($\leq$300 cm^{-1}) by Lorentzian fitting of the experimental Raman data (Fig. 4(b)) where the shift is prominent.

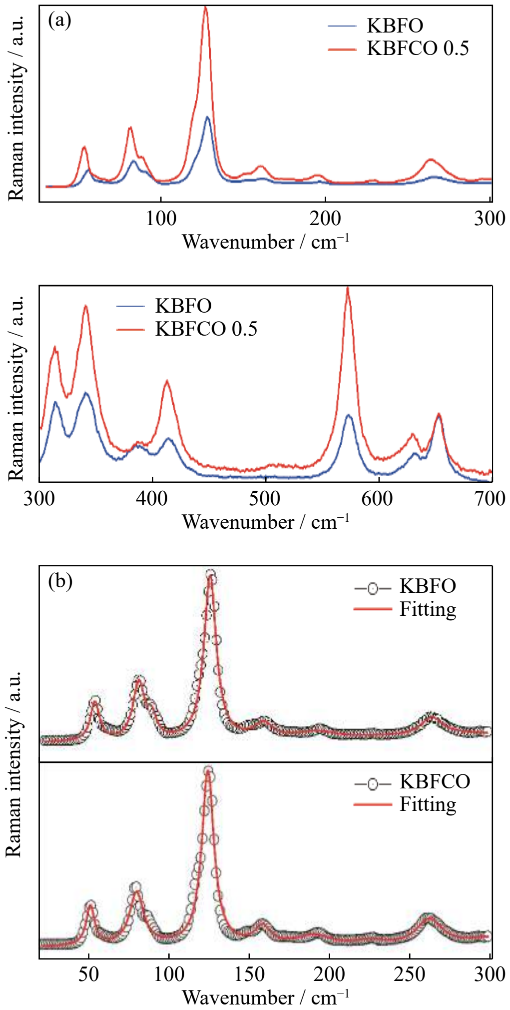

Fig. 4. (a) Room-temperature Raman spectra of pure KBFO (blue) and KBFCO (red) within the wavenumber ranges of 100–300 cm^{-1} (upper half) and 300–700 cm^{-1} (lower half). (b) Lorentzian fitting of the room-temperature Raman spectra of pure KBFO (upper half) and Co-doped KBFO (lower half).

The vibrational modes present at 56 cm^{-1} for pure KBFO can be attributed to Bi–O–Fe and Fe–O–Fe lattice vibrations, which shifted to 53 and 81 cm^{-1} for Co-doped KBFO (Table 3). This observed shift is prominent at 53 cm^{-1} for the Fe–O–Fe vibrational modes of Raman data. This redshift in Raman peaks indicates the changes that occurred in the FeO_4 tetrahedral structure as shown in the Co-doped KBFO crystal structure and can be attributed to the modification in response to oxygen vacancies present in the sample at the time of its preparation [21]. This modification in response to oxy-

Table 3. Room-temperature Raman active vibrational modes

cm^{-1}

Sample	Network mode vibration		Symmetrical stretching	
	Bi–O–Fe	Fe–O–Fe	Bi–O–Fe	Fe–O–Fe
KBFO	56	83	128	162
KBFCO	53	81	127	160

gen vacancies is also reflected in the frequency variation of the dielectric data of the Co-doped KBFO sample.

3.5. Dielectric studies

The room-temperature frequency variation of the dielectric constant (ε') and dielectric loss (Tan δ) of pure and Co-doped KBFO is shown in Fig. 5. The dielectric data of both samples show a similar type of response as a function of frequency at room temperature. Usually, at a low frequency, the high dielectric constant originates from the extrinsic effects (e.g., space charge polarization, Maxwell–Wagner polarization, dipolar polarization, and electronic polarization) [22–23]. The dielectric constant and dielectric loss decrease with the increase in frequency. Notably, at room temperature, the value of the dielectric constant of KBFCO is decreased by approximately 60% in comparison with that of KBFO at 100 kHz. The dielectric loss of KBFCO also decreases in comparison with that of pure KBFO in the low-frequency region. The difference in dielectric loss is significant in the low-frequency regime as the ions have finite time to align themselves in a particular direction of the applied electric field. Co ion substitution at the Fe site affects the charge accumulation in KBFCO, which leads to changes in the values of both dielectric constant and dielectric loss. This decrease in the values of the dielectric constant and dielectric loss of Co-doped KBFO can also be correlated with our room-temperature Raman measurement that indicates the modification in response to oxygen vacancies present in the sample. This modification in response to oxygen vacancies may affect the oxygen trap and conductivity that indicate the decrease in the dielectric constant of Co-doped KBFO, particularly at a lower frequency than that of pure KBFO.

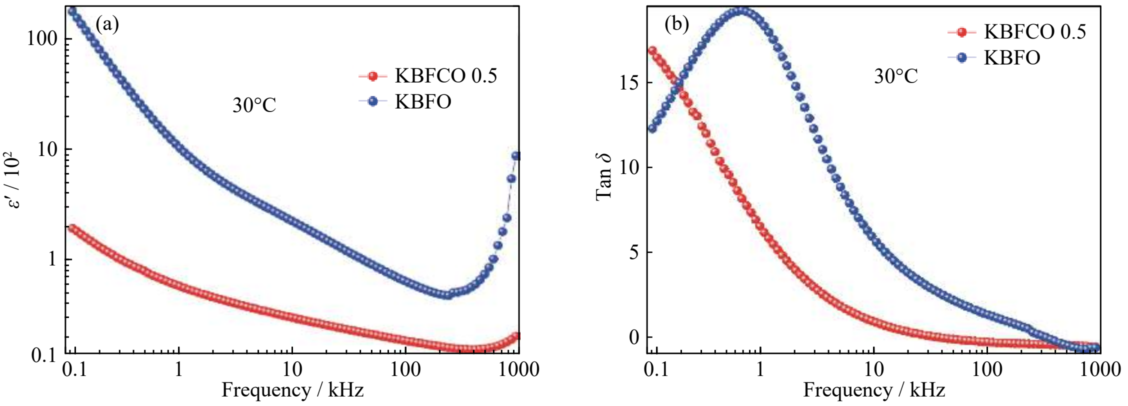

Fig. 5. Frequency variation of the (a) dielectric constant and (b) dielectric loss of KBFO (blue) and KBFCO (red) at room temperature.

3.6. AC electrical conductivity studies

To understand the conduction mechanism of the oxygen trap and its behavior with Co substitution, room-temperature AC electrical conductivity measurement of both pure and Co-doped KBFO samples is conducted, as shown in Fig. 6. AC electrical conductivity is extracted from the room-temperature impedance data using the relation expressed in Eq. (2) [24]:

$$\sigma = \frac{Z'}{[(Z')^2+(Z'')^2]} \times \frac{t}{S} \tag{2}$$

where σ is the AC electrical conductivity, Z' and Z'' are the real and imaginary parts of impedance, respectively, and t and S are the thickness and surface area of the measured samples, respectively. Notably, conductivity increases with the increase in frequency of pure KBFO. At a low electrical frequency (<10 kHz), conductivity becomes independent. However, as frequency further increases, conductivity also increases. Given that pure KBFO has oxygen vacancies, as frequency increases, ion hopping occurs, which drives the conduction mechanism of the sample [25]. However, at a low electrical frequency, the energy for ion hopping is insufficient. Thus, conductivity behaves invariantly with frequency. Co doping modifies the oxygen vacancies present in the sample, thereby affecting the ion hopping process and con-

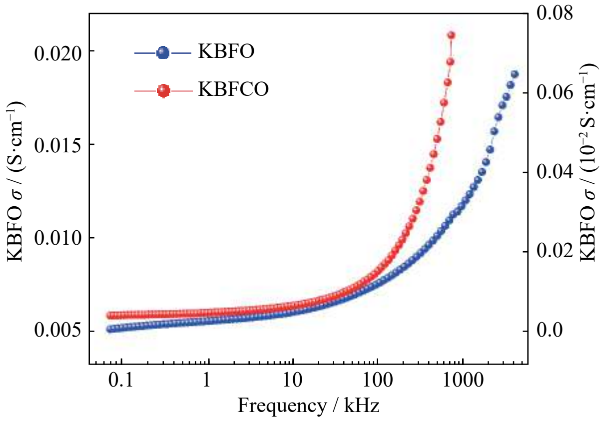

Fig. 6. Frequency dependence of the AC electrical conductivity of pure (blue) and Co-doped KBFO (red) samples at room temperature.

ductivity, as compared with the pure KBFO sample.

4. Conclusion

Here, we successfully synthesized both pure (KBFO) and Co-doped (KBFCO) samples following the solid-state reaction route. The XRD patterns and optical and dielectric properties are investigated carefully. The optical bandgap energy decreased with Co substitution at the Fe site of KBFO. The bandgap energy of KBFO decreased from 1.6 to 1.5 eV. Thus, Co substitution at the Fe site of KBFO leads to the enhancement of its optical properties with the reduction in its bandgap energy. Transition metals, such as Co, in KBFCO enabled the structural modifications, which led to the variation in FeO_4 polyhedra with the modifications in bond angle and bond length, thereby resulting in a considerable change in the bandgap energy. Compared with that in pure KBFO, the Raman active modes in Co-doped KBFO shifted by 3 cm^{-1} toward a lower wavenumber. This redshift in KBFCO indicates the modifications in Fe–O bonds and FeO_4 polyhedra, which may change the oxygen vacancies present in the sample. Both dielectric constant and dielectric loss of KBFCO are reduced to some extent, particularly at the low-frequency region when compared with KBFO. This finding indicates that Co substitution at the Fe site affects the charge accumulation, which decreases the value of the dielectric constant at room temperature. Modification in response to oxygen vacancies is also observed in the measured room-temperature conductivity plot.

Acknowledgements

We acknowledge UGC-DAE CSR, Mumbai (Sanction No. CRS-M-187, 225), Board of Research in Nuclear Science (BRNS), Mumbai (Sanction No. 2012/37P/40/BRNS/2145), and Science and Engineering Research Board (SERB), New Delhi (Sanction No. SR/FTP/PS-187/2011) for funding and fellowships.

References

[1] M. Fiebig, T. Lottermoser, D. Meier, and M. Trassin, The evolution of multiferroics, *Nat. Rev. Mater.*, 1(2016), art. No. 16046.

[2] B. Mettout, P. Tolédano, A.S.B. Sombra, A.F.G. Furtado Filho, J.P.C. do Nascimento, M.A. Santos da Silva, P. Gisse, and H. Vasseur, Magnetoelectric, photovoltaic, and magnetophotovoltaic effects in KBiFe2O5, *Phys. Rev. B*, 93(2016), No. 19, art. No. 195123.

[3] G.H. Zhang, H. Wu, G.B. Li, Q.Z. Huang, C.Y. Yang, F.Q. Huang, F.H. Liao, and J.H. Lin, New high T_c multiferroics $KBiFe_2O_5$ with narrow band gap and promising photovoltaic effect, *Sci. Rep.*, 3(2013), art. No. 1265.

[4] M.A. Jalaja and S. Dutta, Switchable photovoltaic properties of multiferroic $KBiFe_2O_5$, *Mater. Res. Bull.*, 88(2017), p. 9.

[5] D.S. Vavilapalli, K. Srikanti, R. Mannam, B. Tiwari, M.K. K, M.S.R. Rao, and S. Singh, Photoactive brownmillerite multiferroic $KBiFe_2O_5$ and its potential application in sunlight-driven photocatalysis, *ACS Omega*, 3(2018), No. 12, p. 16643.

[6] M.A. Jalaja and S. Dutta, Ferroelectrics and multiferroics for next generation photovoltaics, *Adv. Mater. Lett.*, 6(2015), No. 7, p. 568.

[7] J. Li, G.H. Zhang, L.K. Fan, G.Q. Huang, Z.P. Gao, and T. Zeng, Enhanced visible-light-driven photocatalytic activity of multiferroic $KBiFe_2O_5$ by adjusting pH value, *J. Inorg. Mater.*, 33(2018), No. 7, art. No. 805.

[8] D.S. Vavilapalli, A.A. Melvin, S. Kavita, A.K. Yadav, S.N. Jha, D. Bhattacharyya, S.C. Sarma, S.C. Peter, M.S. Ramachandra Rao, and S. Singh, Multifunctional brownmillerite $KBiFe_2O_5$: Structural, magneto-dielectric, optical, photoelectrochemical studies and enhanced photocatalytic activity over perovskite $BiFeO_3$, *Sol. Energy Mater. Sol. Cells*, 200(2019), art. No. 109940.

[9] Q.Y. Xu, H.F. Zai, D. Wu, T. Qiu, and M.X. Xu, The magnetic properties of $Bi(Fe_{0.95}Co_{0.05})O_3$ ceramics, *Appl. Phys. Lett.*, 95(2009), No. 11, art. No. 112510.

[10] Y.S. Chiang, C.S. Tu, P.Y. Chen, C.S. Chen, J. Anthoniappen, Y. Ting, T.S. Chan, and V.H. Schmidt, Magnetic and phonon transitions in B-site Co doped $BiFeO_3$ ceramics, *Ceram. Int.*, 42(2016), No. 11, p. 13104.

[11] U. Khan, N. Adeela, K. Javed, S. Riaz, H. Ali, M. Iqbal, X.F. Han, and S. Naseem, Influence of cobalt doping on structural and magnetic properties of $BiFeO_3$ nanoparticles, *J. Nanopart. Res.*, 17(2015), art. No. 429.

[12] H.M. Rietveld, A profile refinement method for nuclear and magnetic structures, *J. Appl. Crystallogr.*, 2(1969), No. 2, p. 65.

[13] M. Zhang, Z.H. Wang, S.Y. Lin, Y. Wang, and Y.H. Pan, Investigation on a new multiferroic compound $KBiFe_2O_5$: Structural, optical, electrical and magnetic properties, *J. Alloys Compd.*, 699(2017), p. 561.

[14] X.Z. Zhai, H.M. Deng, W.L. Zhou, P.X. Yang, J.H. Chu, and Z. Zheng, Structural, optical and magnetic tunability in $KBiFe_2O_5$ multiferroics, *RSC Adv.*, 5(2015), No. 100, p. 82351.

[15] M.M. Rhaman, M.A. Matin, M.N. Hossain, F.A. Mozahid, M.A. Hakim, and M.F. Islam, Bandgap engineering of cobalt-doped bismuth ferrite nanoparticles for photovoltaic applications, *Bull. Mater. Sci.*, 42(2019), art. No. 190.

[16] D.L. Wood and J. Tauc, Weak absorption tails in amorphous semiconductors, *Phys. Rev. B*, 5(1972), No. 8, p. 3144.

[17] X.Z. Zhai, H.M. Deng, W.L. Zhou, P.X. Yang, J.H. Chu, and Z. Zheng, Optical and magnetic properties of $KBiFe_2O_5$ thin films fabricated by chemical solution deposition, *Mater. Lett.*, 161(2015), p. 423.

[18] R. Rai and M. Molli, Effect of La doping on structural, magnetic, and optical properties of $KBiFe_2O_5$, *J. Mater. Sci.: Mater. Electron.*, 30(2019), No. 4, p. 4318.

[19] A. Sarkar and G.G. Khan, The formation and detection techniques of oxygen vacancies in titanium oxide-based nanostructures, *Nanoscale*, 11(2019), No. 8, p. 3414.

[20] G.H. Zhang, F.L. Liu, T.T. Gu, Y.S. Zhao, N.N. Li, W.G. Yang, and S.H. Feng, Ferroelectrics: enhanced ferroelectric and visible-light photoelectric properties in multiferroic $KBiFe_2O5$ via pressure-induced phase transition (*Adv. Electron. Mater.* 3/2017), *Adv. Electron. Mater.*, 3(2017), No. 3.

[21] W.W. Mao, X.F. Wang, Y.M. Han, X.A. Li, Y.T. Li, Y.F. Wang, Y.W. Ma, X.M. Feng, T. Yang, J.P. Yang, and W. Huang, Effect of Ln (Ln = La, Pr) and Co co-doped on the magnetic and ferroelectric properties of $BiFeO_3$ nanoparticles, *J. Al-*

loys Compd., 584(2014), p. 520.

[22] A. Singh, R. Chatterjee, S.K. Mishra, P.S.R. Krishna, and S.L. Chaplot, Origin of large dielectric constant in La modified $BiFeO_3$–$PbTiO_3$ multiferroic, *J. Appl. Phys.*, 111(2012), No. 1, art. No. 014113.

[23] J.J. Liu, C.G. Duan, W.G. Yin, W.N. Mei, R.W. Smith, and J.R. Hardy, Large dielectric constant and Maxwell–Wagner relaxation in $Bi_{2/3}Cu_3Ti_4O_{12}$, *Phys. Rev. B*, 70(2004), No. 14, art. No. 144106.

[24] M.M. Hoque, A. Dutta, S. Kumar, and T.P. Sinha, Dielectric relaxation and conductivity of $Ba(Mg_{1/3}Ta_{2/3})o_3$ and $Ba(Zn_{1/3}Ta_{2/3})o_3$, *J. Mater. Sci. Technol.*, 30(2014), No. 4, p. 311.

[25] A.L. Si, M. Kiani, and S, Rizwan, Structural, magnetic and dielectric properties of Sm^{3+} and Mn^{2+} co-doped $BiFeO_3$ nanoparticles, *J. Powder Metall. Min.*, 6(2017), No. 1, p. 1.